ACS APPLIED MATERIALS & INTERFACES

www.acsami.org

Research Article

Highly Ordered, Plasmonic Enhanced Inverse Opal Photonic Crystal for Ultrasensitive Detection of Staphylococcal Enterotoxin B

Huijing Shen,[#] Jialei Bai,[#] Xudong Zhao, Beibei Lu, Dianpeng Han, Shuang Li, Kang Qin, Shuyue Ren, Yu Wang, Minglin Wang, Yujing Lian,* Zhixian Gao,* and Yuan Peng*

Cite This: *ACS Appl. Mater. Interfaces* 2022, 14, 4637−4646

Read Online

ACCESS | Metrics & More | Article Recommendations | Supporting Information

ABSTRACT: Although there is considerable interest in self-assembly of ordered, porous "inverse opal" structures for optical, electronic, and chemical applications, uncontrolled defect formation limits the usefulness of such materials. Herein, we develop a highly ordered and plasmonic enhanced sensing inverse opal photonic crystal (IOPC) material. The co-assembly of the colloidal template with the matrix material avoids the need for liquid penetration into the preassembled colloidal crystals and minimizes the associated rupture and inhomogeneity of the resulting IOPC. Au nanoparticles (Au NPs) not only act as a "bridge" between recognition elements (aptamers) and IOPCs, but also can amplify optical signals. Furthermore, the enhancement mechanism of Au NPs is simulated by COMSOL. During the detection process, the optical signal of the sensing Au−Apt IOPC responds to the Staphylococcal enterotoxin B with a concentration ranging from 10^{-2} to 10^{3} pg mL^{-1}, and the limit of detection is 2.820 fg mL^{-1}. Spiked real sample detection indicates that the as-proposed method possessed good accuracy. The sensing Au−Apt IOPC provides an extensive biosensor platform to detect a variety of toxic and harmful substances through replacing the aptamer by other recognition elements, such as antibodies or receptors.

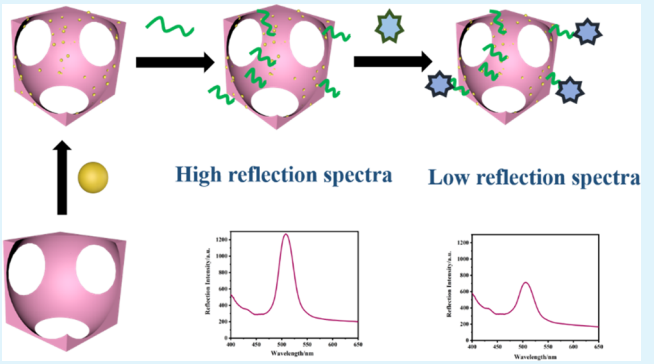

KEYWORDS: *inverse opal photonic crystal, Au nanoparticle, localized surface plasmon resonance, signal enhancement, ultrasensitive detection*

INTRODUCTION

Nature creates complex microstructures with advanced functionality by controlling the chemistry and morphology of the nanoscale building blocks. However, their formation in artificial self-assembly systems is challenging as it involves a complex interplay of competing forces during and after assembly. For example, in the preparation of the inverse opal photonic crystal (IOPC), colloidal assembly requires fine-tuning of factors such as the size and surface charge of the particles and electrolyte strength of the solvent to enable successful self-assembly and minimize crack formation.[1] The IOPC is a three-dimensional (3D) PC with regular porous array structures using a colloidal crystal as the template.[2−4] These 3D porous structures have received significant attention due to their unique physicochemical, optical, and mechanical properties,[3,5,6] especially merits in structural regularity and interconnectivity.[5−7] Current research studies indicated that a high degree of control over their composition and quality is important for many of their applications, including medicine,[7] photoelectric science,[8] and energy science.[9] Structural defects, such as cracks, will be detrimental to IOPC's performance, as they lead to optical scattering and escape paths. In order to avoid such defects, nature often utilizes soft, typically organic entities to direct the deposition of inorganic materials.[10] Inspired by this strategy, we adopted Hatton's co-assembly method[11] to prepare highly ordered, crack-free inverse opal films. Multilayer composite colloidal crystal films are formed by evaporation deposition of polymer microspheres suspended in hydrolyzed silicate sol gel precursor solution. The co-assembly of the colloidal template and matrix material avoids the process of liquid penetration into the preassembled opal crystals and minimizes the associated cracks and inhomogeneity of the resulting IOPC films.

Sensing materials, based on IOPC films, have the advantage of low cost, efficiency, and accuracy and have been favored by researchers in recent years.[12,13] However, how to improve the attachment of the recognition elements efficiently and enhance the detection signal are still challenges.[14,15] Au nanoparticles (Au NPs) have attracted extensive interest due to their

Received: September 23, 2021
Accepted: December 30, 2021
Published: January 13, 2022

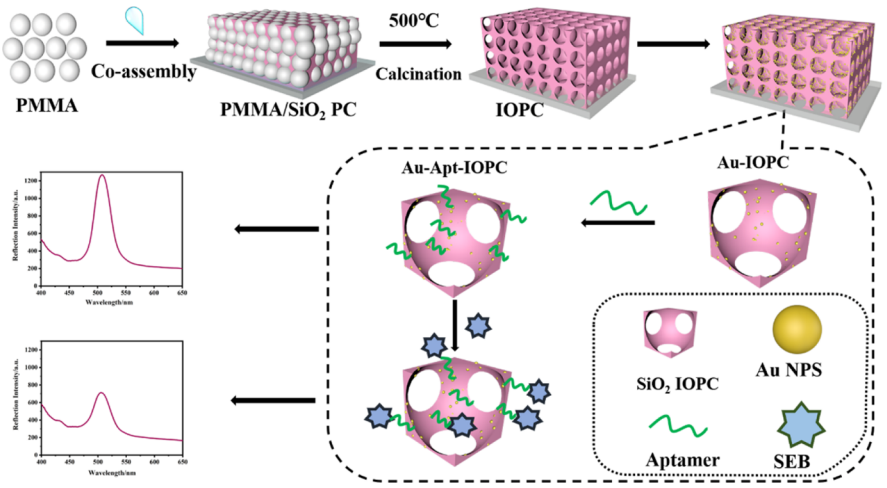

Figure 1. Schematic illustrations of the preparation and detection procedure of the Au−Apt IOPC.

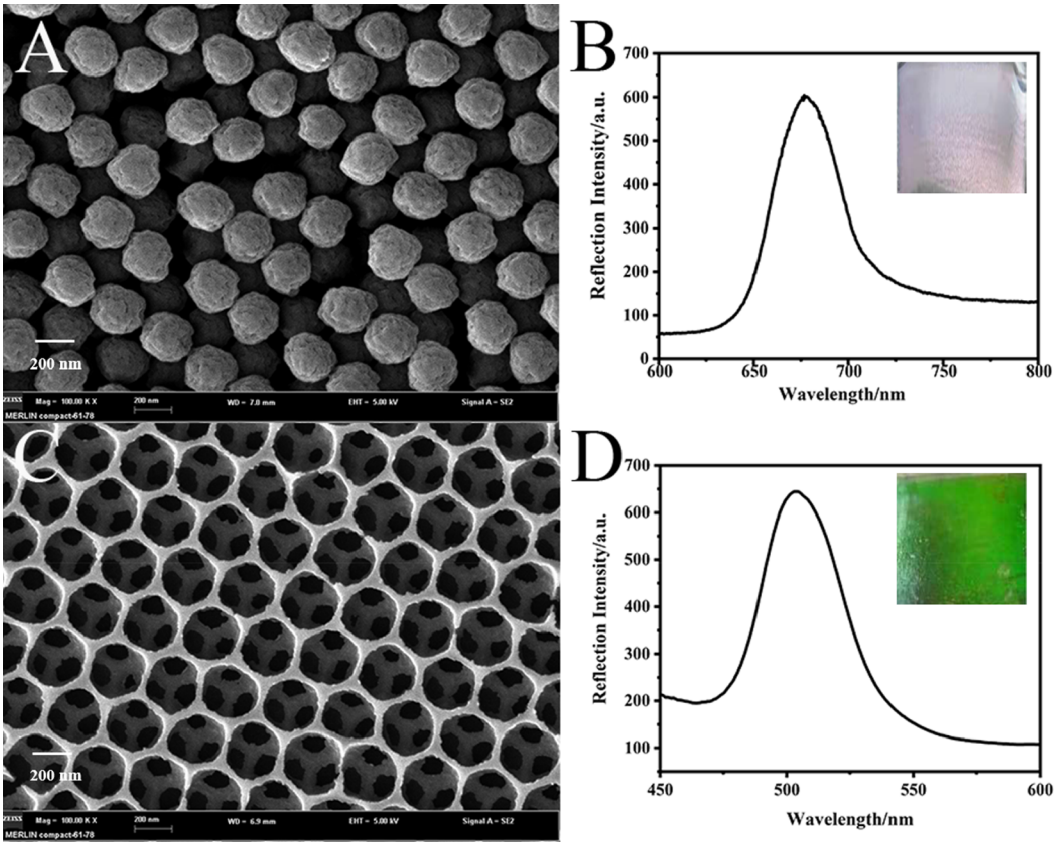

Figure 2. (A) Top view of the PMMA/SiO_2 PC (90 μL of silica gel and 0.9% of PMMA microsphere suspension were co-assembled at 60 °C for 48 h); (B) reflection spectra of the PMMA/SiO_2 PC (λ = 680 nm; inset: optical image of the red PMMA/SiO_2 PC); (C) top views of the SiO_2 IOPC obtained by removing PMMA at 500 °C for 4 h; and (D) reflection spectra of the SiO_2 IOPC (λ = 510 nm; inset: optical image of the green IOPC). The scale bar is 200 nm.

advanced properties and have been widely used in the fields of catalysis,[16] sensing,[17−20] and solar cells.[21,22] Furthermore, their unique properties could strongly enhance the optical process, leading to the signal amplification. This phenomenon is due to the effect of localized surface plasmon resonance (LSPR) caused by the collective vibration of surface electrons excited by incident light. In particular, Au NPs combined with the IOPC had been used for catalysis,[23] or assay,[24] and the Au−IOPC material had good performance. However, the preparation process was more cumbersome and required professional equipment. Furthermore, the modification of Au on the abovementioned surface of the IOPC resulted in limited binding sites. Therefore, the Au−IOPC material needs more improvement.

Staphylococcus aureus causes various human diseases by secreting virulence factors called Staphylococcal superantigens.[25] Staphylococcal enterotoxin B (SEB) is one of the staphylococcal super antigens responsible for food poisoning in humans, which can cause acute gastroenteritis and sepsis. Because of its extremely low lethal dose (LD_{50} = 20 ng kg^{-1})

https://doi.org/10.1021/acsami.1c18386
ACS Appl. Mater. Interfaces 2022, 14, 4637−4646

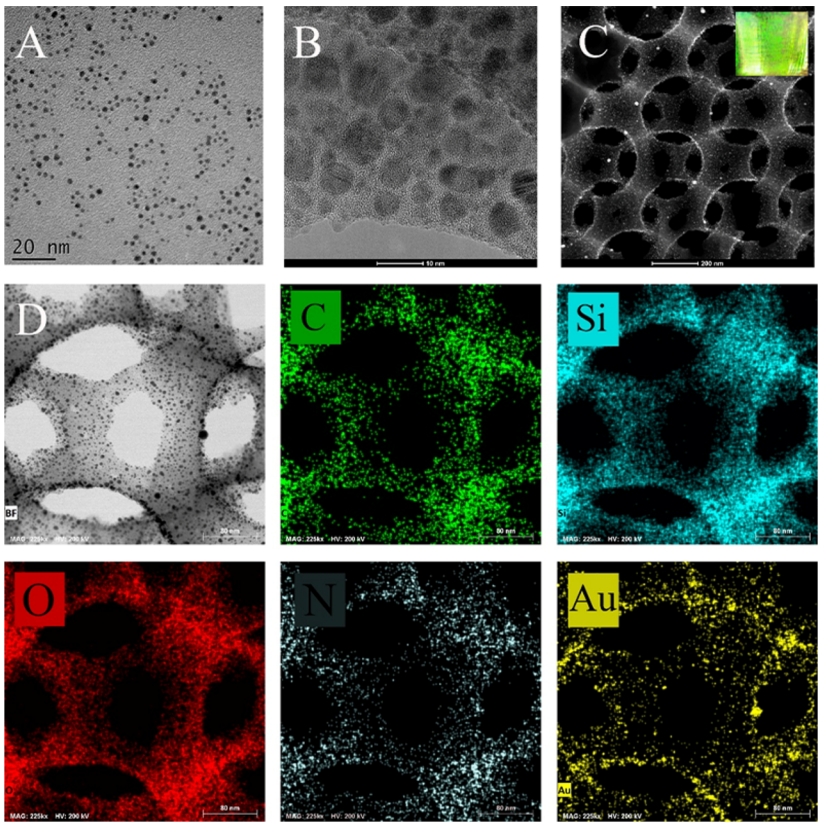

Figure 3. TEM of Au NPs and elemental mapping images of the IOPC. (A) TEM image of Au NPs (5−8 nm) obtained by Duff's method. (B) Magnified area of the Au−IOPC; The scale bar is 10 nm. (C) TEM of the Au−IOPC (inset: optical image of the Au−IOPC with emerald metallic luster). The scale bar is 200 nm. (D) Elemental mapping images of the Au−IOPC, including C, Si, O, N, and Au. The scale bar is 80 nm.

and great harm that it inflicts, it is listed in the International Convention on the Prohibition of Chemical Weapons.[26] Therefore, it is necessary to develop a label-free, simple, and ultrasensitive detection method.

Herein, a sensing material was designed, which was prepared by the SiO_2 IOPC modified with Au NPs. The seamless IOPC thin films were prepared by co-assembly of PMMA (polymethyl methacrylate) and SiO_2, followed by removing the template (PMMA microspheres) through calcination. Au NPs were introduced into the IOPC to form the Au−IOPC, and SEB aptamers (containing 5′-terminated sulfhydryl groups), used as the recognition element, were immobilized on Au NPs by the Au−S bond to obtain the sensing material (Au−Apt IOPC). During the detection process, the intensity of the Au−Apt IOPC reflection peak decreased when the aptamer combined with SEB, thereby realizing the ultrasensitive detection. The combination of Au NPs with the IOPC is prospective not only to simplify the complicated preparation steps, but also to amplify the optical response signals. The preparation and detection procedure of the sensing Au−Apt IOPC is shown in Figure 1.

RESULTS AND DISCUSSION

Characterizations of PMMA Microspheres and IOPCs. PMMA/SiO_2 colloidal crystals and IOPCs were characterized by scanning electron microscopy (SEM) using Zeiss Merlin Compact. The SEM results are shown in Figure 2. The PMMA microspheres prepared by soap-free polymerization were stable and uniformly dispersed (Figure S1). This was because MMA was hydrophobic and would form small droplets after being stirred, and then the surface tension of the hydrophobic droplets would make it spherical. The uniform particle size of the PMMA microsphere laid a good foundation for the co-assembly of PMMA and SiO_2 colloidal crystals. Figure 2A shows SEM images of the overhead plane of the PMMA/SiO_2 colloidal crystal, indicating that the desired product was achieved through the effectively co-assembly method.

The IOPC films was obtained by removing the PMMA template from the PMMA/SiO_2 colloidal crystal at high temperature (Figure 2C). The top view of the IOPC showed that it had 3D ordered periodic structures with interconnected macroporous. This periodic macroporous structures provided sufficient space for the diffusion of macromolecules.

This highly ordered macroporous structure significantly expanded the specific surface area without cracks. The feature of the crack-free structure was important because cracks might induce Au NP aggregation, leading to a change in the coupling of the plasma resonance between adjacent particles and ultimately a wavelength shift at the formant.[27] The photonic band gaps (PBGs) of the PMMA/SiO_2 PC and IOPC recorded by the Ocean Optical Maya 2000 Pro fiber optic spectrometer (Ocean Optics, Dunedin, FL, USA) were located at 680 nm and 510 nm, respectively (Figure 2B,D). In addition, compared with the PMMA/SiO_2 PC, the IOPC showed a significant blue shift of the PBG, turning from red to green. The change of the PC structural color was attributed to the replacement of the PMMA spheres by air with a lower refractive index, thus reducing the refractive index of the PC. The maximum diffraction wavelength (λ_{max}) of the PMMA/SiO_2 PC and IOPC followed Bragg's law

https://doi.org/10.1021/acsami.1c18386
ACS Appl. Mater. Interfaces 2022, 14, 4637−4646

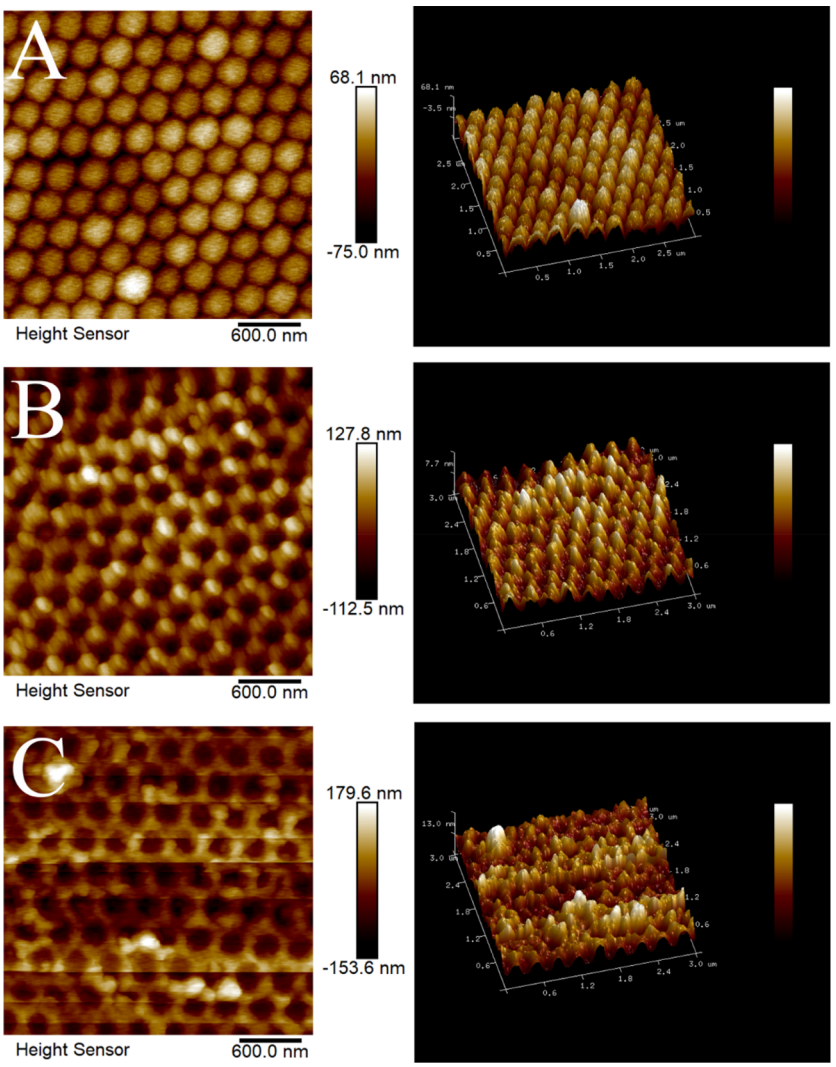

Figure 4. AFM images of (A) PMMA/SiO_2 PC, (B) Au−Apt IOPC, and (C) Au−Apt-SEB IOPC. The scale bar is 600 nm.

$$\lambda_{max} = 1.633(d/m)(D/D_0)(n_{eff}^2 - \sin^2\theta)^{1/2} \quad (1)$$

$$n_{eff} = [n_1^2 f + n_2^2(1-f)]^{1/2} \quad (2)$$

d is the planar spacing, m is the order of Bragg diffraction (here $m = 1$), n_{eff} is the effective refractive index (ERI) of the PC under given conditions, $D/D_0 = 1$ is the swelling ratio of the PC, θ is the angle of the incident light and the normal of the crystal surface (here, $\theta = 0$).[28]

A close-packed array was assumed, and the volume fraction f was 0.74. For the PMMA/SiO_2 PC, n_{eff} was the ERI of PMMA particles (n_1, 1.48) and SiO_2 (n_2, 1.65), while for the SiO_2 IOPC, n_{eff} was the ERI of SiO_2 (n_1, 1.65) and air (n_2, 1.00). The theoretical values of λ_{max} of the PMMA/SiO_2 PC and SiO_2 IOPC were calculated by eqs 1 and 2, and the results were 673 and 517 nm, respectively. λ_{max} of the PMMA/SiO_2 PC was observed by in the visible spectral region. After removing the PMMA array, the λ_{max} of the SiO_2 IOPC was 510 nm. The theoretical calculations are consistent with the experimental results.

Under high-resolution transmission electron microscopy (TEM) images (Titan cubic Themis G2 300), the periodic 3D Au−IOPC matrix was dotted with numerous tiny black spots, which was the Au NPs modified in the IOPC (Figure 3B−D). The particle size of Au NPs was uniform and was about 5−8 nm. The LSPR absorption spectra of Au NPs were determined by an UV−vis spectrophotometer (TU-1901, Persee Co., Ltd., Beijing, China). As shown in Figure S4, the maximum absorption wavelength was about 520 nm, which was basically close to the PBG of the IOPC. Figure 3B shows the edge of the prepared Au−IOPC hole, and the uniform AuNPs on the surface could be clearly observed, indicating that Au NPs were modified on the IOPC.

The TEM image of the Au−IOPC is shown in Figure 3C, and it showed that regular arrangement of this microporous structure of the Au−IOPC provided a sufficient space for the diffusion of the targets and, meanwhile, supplied an abundant surface for the extensive modification of Au NPs.[29] The illustration was the optical picture of the Au−IOPC. The color of the Au−IOPC presented an emerald metallic luster, which indicated that Au NPs had been successfully modified on the IOPC. Meanwhile, the reflection peak intensity of the Au−IOPC was enhanced by Au NPs (Figure S3). Furthermore, the C, N, O, Au, and Si elements were clearly visible in the elemental mapping image (Figure 3D). The distribution of N and Au elements was completely along with the IOPC skeleton, indicating that these elements were attached on the

https://doi.org/10.1021/acsami.1c18386
ACS Appl. Mater. Interfaces 2022, 14, 4637−4646

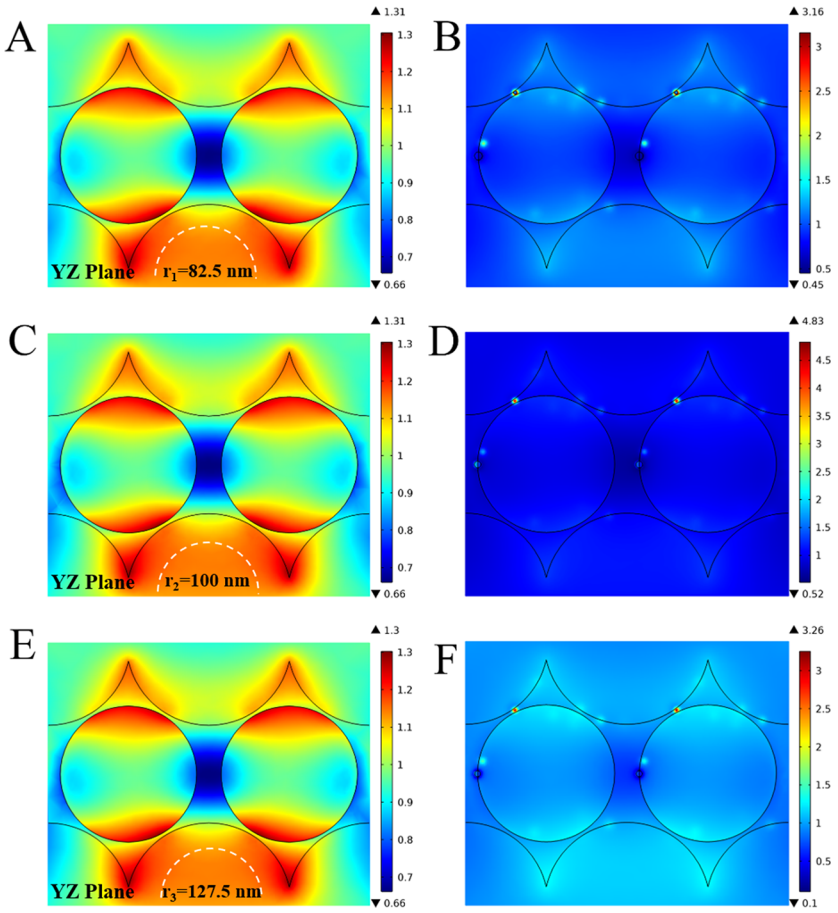

Figure 5. Simulated comparison between the IOPC and Au−IOPC. (A) IOPC (d = 165 nm, λ = 435 nm), (B). Au−IOPC (d = 165 nm, λ = 435 nm), (C) IOPC (d = 200 nm, λ = 515 nm), (D) Au−IOPC (d = 200 nm, λ = 435 nm), (E) IOPC (d = 255 nm, λ = 590 nm), and (F) Au−IOPC (d = 255 nm, λ = 590 nm), r: the radius of the air sphere, YZ plane.

IOPC skeleton. The results showed the successful modification of the amino group and the Au element.

The X-ray photoelectron spectroscopy (XPS, ESCALAB 250Xi) results further proved the successful modification of $-NH_2$, Au NP, and aptamer (Figure S5). Compared with the IOPC, NH_2−IOPC had an obvious N peak at 400 eV, which indicated the successful introduction of amination. Moreover, the Au−IOPC had a Au peak (BE = 87 eV), which indicated that the Au NPs were successfully attached on the IOPC. After the aptamer was added on the surface of the Au−IOPC, the appearance of the P 2p (BE = 133.08 eV) peak represented the existence of the aptamer phosphate group, and the S 2p (BE = 168.14 eV) peak indicated the existence of the mercapto group modified at the 5′ end of the aptamer, which fully demonstrated the successful modification of the aptamer.

Sensing Feasibility of the Au−Apt IOPC. The Au−IOPC was immersed in deionized water and placed below the optical probe until the sensing system stabilized before SEB detection. Then, different concentrations of SEB were added, and corresponding reflectance spectra were recorded. Figure S8A shows that with the increasing SEB concentration, the reflection spectrum of the Au−IOPC remained almost constant. Meanwhile, the Au−Apt IOPC was used to detect SEB as the same method, and the increasing SEB could cause the decrease of the reflection peak intensity (Figure S8B). This phenomenon illustrated that Au−IOPC without the recognition element, aptamer, would not respond to the target, SEB. In other words, SEB could not nonspecifically bind to the Au−IOPC without the aptamer.

The morphology of PMMA/SiO_2 PC films, Au−Apt IOPC and Au−Apt IOPC, after detecting SEB (Au−Apt-SEB IOPC) was characterized by atomic force microscopy (AFM, Dimension FastScan, Bruker, the United States). The PMMA/SiO_2 PC shown in Figure 4A presented a regular periodic array structure and was composed of tightly packed solid spheres. After removing PMMA and modifying the aptamer, the surface of the IOPC could be observed to have lots of holes like a honeycomb structure, and the surface roughness increased compared with the PMMA/SiO_2 PC. However, its rough surface was relatively uniform (Figure 4B). After SEB detection, the array structure of the sensing material became irregular and the surface roughness turned confusing (Figure 4C). This indicated that during the SEB detection, SEB was combined to the sensing Au−Apt IOPC through the aptamer, leading to the damage of the periodic structure, which was also the root cause of the decrease in the intensity of the reflection peak.

COMSOL Simulation of LSPR for Different Sizes. In order to investigate the electromagnetic field (EM) interaction of IOPCs and Au NPs, COMSOL Multiphysics, a commercial software based on finite element methods, was used to characterize the local electromagnetic distributions in the Au−IOPC. The EM vector Helmholtz equation was as follows

https://doi.org/10.1021/acsami.1c18386
ACS Appl. Mater. Interfaces 2022, 14, 4637−4646

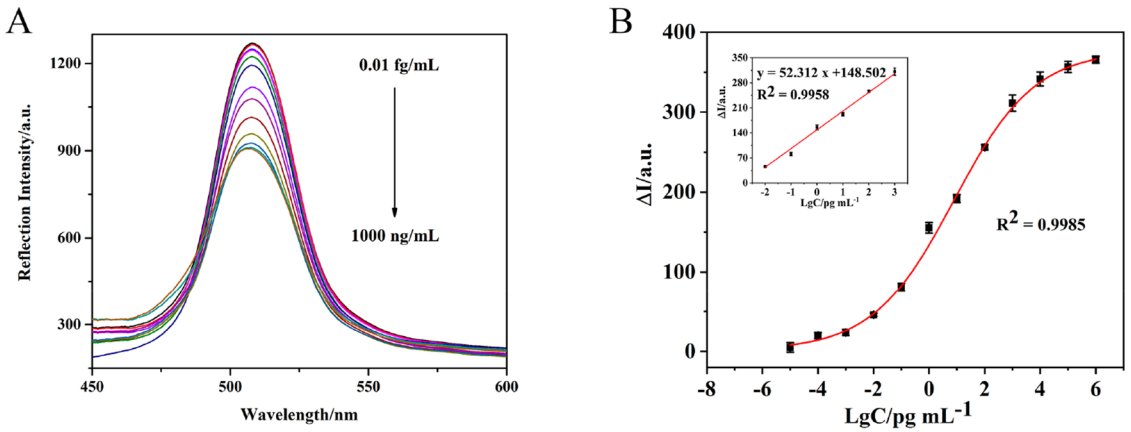

Figure 6. (A) Optical responses of the Au−Apt IOPC to different SEB concentrations (from 0.01 fg mL^{-1} to 1000 ng mL^{-1}); (B) standard curve of SEB detection (inset: linear relationship between the peak intensity changes and logarithm concentration of SEB). The averaged values and standard deviations were calculated from three replicated measurements.

$$\nabla \times (\nabla \times \mathrm{EM}) - k_0^2 \varepsilon_r \mathrm{EM} = 0 \quad (3)$$

$k_0 = 2\pi/\lambda$, and it is the wavenumber in the vacuum, and λ is the wavelength of the incident light. ε_r is the relative dielectric constant of the materials. A plane light wave with the amplitude (E_0) of 1 V/m was incident along the direction of *Z*-axis and had a polarization in the *X*-axis direction. The refractive index of the Au NP material was according to the value reported by Johnson and Christy.[30] The refractive index of silicon dioxide (SiO_2) was according to the value reported by Gao et al.[31] The wavelength of the incident light was set according to the PBG of the IOPC.

Figure 5A,C,E shows the normalized EM distribution of the IOPC without Au NPs under different incident lights of wavelengths at 435, 515, and 590 nm, respectively. These results showed the distribution of the EM in the IOPC, and energy hotspots could be observed in the array structure. In order to investigate the interaction between the ordered IOPC and Au NPs, the surface of IOPC was modified with 5−8 nm Au NPs, and the EM was resimulated. The results (Figure 5B,D,F) showed that the EM was redistributed in the Au NPs−IOPC and exhibited energy hotspots near the IOPC skeleton and on the Au NPs (bright dots in Figure 5B,D,F). Furthermore, the EM amplitude of the Au NPs−IOPC exhibited an approximately twofold enhancement compared with the EM amplitude of the IOPC. Especially in Figure 5D, Au−IOPC maximum EM enhancement ($|E|/|E_0|$) was 4.83, where the intensity ($|E|^2/E_0|^2$) of the diffraction optical signal could be increased by 4.83^2 times. This might be because the wavelength of the incident light (515 nm) was close to the absorption wavelength of the Au NPs, which caused the LSPR of the Au NPs. The LSPR effect enhanced the EM around the IOPC, resulting in the amplification of the optical signal.[31] The wavelength of the incident light at 435 nm (Figure 5B) and 590 nm (Figure 5F) could not cause the LSPR effect because they were out of the absorption spectrum of Au NPs. This simulation was just a preliminary investigation. The amount of Au NPs in this simulation was far less than that observed in TEM. As the amount of Au NPs increased, the amount of calculation was extremely large, because of which the simulation could not be continued. This required further research. In addition, 3D models of the simulated unit diagram of the IOPC and Au−IOPC are shown in Figure S7. Figure 5 shows a cross-section result of Figure S7.

Optical Response of the Au−Apt IOPC to Analytes. As shown in Figure S9A, after the reaction of the aptamer and Au−IOPC, the UV absorption peak of the aptamers obviously decreased, indicating that the aptamers were successfully modified onto the Au−IOPC. Furthermore, the concentration of the aptamer was one of the most important conditions affecting the response of the sensing Au−Apt IOPC to SEB. Thus, four SEB aptamer concentrations, 1, 5, 10, and 20 μM, were chosen to be modified on the Au−IOPC, and the corresponding sensing Au−Apt IOPC was used to detect series SEB. According to the results (Figure S9B), the sensing Au−Apt IOPC acquired by the 10 μM aptamer showed more obvious signal change and wider detection range. Then, 10 μM was chosen as the optimal concentration for further experiments.

The response dynamics of Au−Apt IOPC to SEB was investigated. After SEB was added to the sensing system, the reflection peak intensity was recorded every minute. The results showed that once SEB was added, the peak intensity would decrease. After 30 min, the peak intensity no longer decreased and tended to be stable (Figure S6).

After the Au−Apt IOPC was stable in deionized water, different concentrations of SEB (0.01 fg mL^{-1} to 1000 ng mL^{-1}) were added, and the corresponding reflection spectrum was obtained by a fiber spectrophotometer.

As shown in Figure 6A, the peak intensity decreased gradually, as the SEB concentration increased. The Au−Apt IOPC was obtained by high-temperature calcination, and it was too rigid to be strained. The combination of the aptamer and SEB could not cause the even change of the lattice structure, but caused the periodic array to be irregular. Therefore, it led to the decrease of reflection intensity rather than the spectral shift. Meanwhile, it had been reported that the reflection intensity of sensing photonic crystals could decrease with the increase of target concentration.[32,33] A distinct ΔI about 10 a.u. could be observed directly, when the concentration of SEB was as low as 0.01 fg mL^{-1}, indicating the high sensitivity of the Au−Apt IOPC.

A relationship had been obtained between the ΔI of reflection peak intensity and logarithm of SEB concentration (log *C*) (Figure 6A), in which y is ΔI and *x* is Lg *C* (pg mL^{-1}). Simultaneously, ΔI showed a good linear relationship with the Lg *C* in the range from 10^{-2} to 10^3 pg mL^{-1} (Figure 6B, inset), and the regression equation was $y = 52.312x + 148.502$ (R^2 =

https://doi.org/10.1021/acsami.1c18386
ACS Appl. Mater. Interfaces 2022, 14, 4637−4646

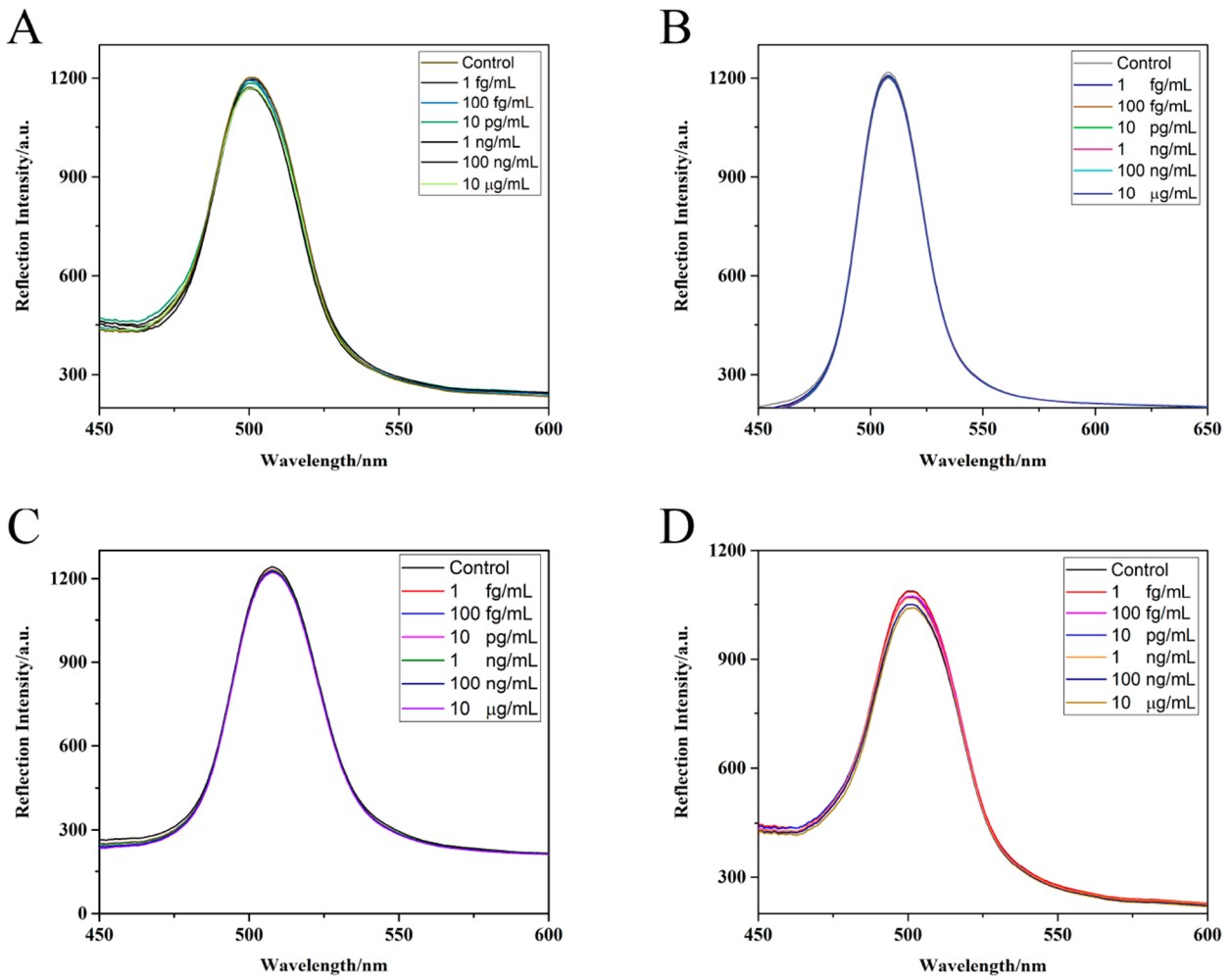

Figure 7. Optical response of the sensing Au–Apt IOPC to (A) SEA, (B) ricin toxin, (C) BSA, and (D) OVA.

Table 1. Recovery Assay for SEB in Milk and Water

		Au–Apt IOPC			ELISA kit		
sample	spiked (pg mL^{-1})	found[a] (pg mL^{-1})	recovery (%)	RSD (%)	found[a] (pg mL^{-1})	recovery (%)	RSD (%)
milk	0	Nd*			Nd		
	0.1	0.093	93.0	3.2	Nd		
	10	11.54	115.4	2.4	11.16		
	100	104.53	104.5	4.3	116.93	116.9	7.9
tap water	0	Nd			Nd		
	0.1	0.089	89.0	2.5	Nd		
	10	9.57	95.7	2.6	10.95		
	100	102.38	102.4	4.6	112.82	112.8	12.4

[a]n = 3, each spiked concentration was obtained from three parallel experiments. *Nd: not detected.

0.9958). The limit of detection (LOD) was about 2.820 fg mL^{-1}, which was far below the detection limits of some other methods such as high-performance liquid chromatography–diode array detector,[34] immunochromatographic method,[35] and SPR.[36]

The CHO–Apt IOPC was used to detect SEB as a comparison. After SEB was added in the sensing system, the peak intensity also decreased gradually with the increasing concentration of SEB (Figure S10A). It showed a linear relationship between ΔI and Lg C in the SEB concentration range from 10^{-1} to 10^{3} pg mL^{-1} (Figure S10B), and the regression equation is $y = 22.232x + 44.355$ with $R^2 = 0.9960$. The LOD of CHO–Apt IOPC was 37.14 fg mL^{-1}.

The results showed that Au–Apt IOPC was more sensitive than CHO–Apt IOPC due to the LSPR effects of Au NPs immobilized onto the inner surface of the IOPCs. Meanwhile, the introduction of Au NPs could provide more binding sites, which increased the amount of the SEB aptamer fixed on the IOPC. Furthermore, the preparation process of the Au–Apt IOPC was simpler than that of the traditional IOPC (CHO–Apt IOPC) without Au NPs.

Specificity of the Au–Apt IOPC to Analytes. The specificity of the sensing Au–Apt IOPC for the SEB target was

https://doi.org/10.1021/acsami.1c18386
ACS Appl. Mater. Interfaces 2022, 14, 4637–4646

investigated under the same conditions. The SEB analogues (concentration from 1 fg mL^{-1} to 10 μg mL^{-1}), such as SEA, ricin toxin, bovine serum albumin (BSA), and OVA, were detected by the as-proposed method. The reflection spectra are shown in Figure 7. The Au−Apt IOPC scarcely presented response to SEA, ricin toxin, BSA, and OVA (Figure 7A−D). This result indicated that the Au−Apt IOPC showed excellent specificity for SEB.

Real Sample Analysis. Milk and water samples spiked with SEB (0, 0.1, 10, and 100 pg mL^{-1}) were detected by this as-proposed method, respectively. Meanwhile, these samples were analyzed using a commercial ELISA kit to evaluate the accuracy and sensitivity of the IOPC method in real samples.

As listed in Table 1, the recoveries obtained by the sensing Au−Apt IOPC method were from 92.9 to 115.4%, and the RSD (n = 3) was below 5%. Meanwhile, the LOD of the SEB ELISA kit was 0.1 ppb, and it could not determine SEB concentration in the samples spiked with 0.1 and 10 pg mL^{-1} SEB. These results indicated that the as-proposed sensing Au−Apt IOPC method showed good accuracy and possessed a wider detection range. Furthermore, it had potential application in ultrasensitive detection of SEB in real samples without the label.

CONCLUSIONS

In conclusion, a sensing Au−Apt IOPC films were prepared by the co-assembly method, and the aptamer was used as recognition elements to realize ultrasensitive detection of SEB. Au NPs modified on the IOPC played a role in signal enhancement to improve the detecting sensitivity. Furthermore, Au NPs were used as a bridge to connect the aptamer with the IOPC. The constructed sensing Au−Apt IOPC could respond to SEB within 30 min and possessed good specificity. Compared with the conventional method, the detection limit obtained by this method was several orders of magnitude lower, and the detection limit was 2.820 fg mL^{-1}. In addition, the preparation of the Au−IOPC based on the LSPR sensor was simple and environmentally friendly, requiring very little organic solvent in the preparation and detection process. Furthermore, if the rigid skeleton structure is replaced by compliant materials, and it will be expected to achieve visual detection caused by the structure color change. Thus, it is possible to obtain the POC testing device for environmental monitoring, clinical diagnosis, and so forth.

EXPERIMENTAL SECTION

Reagents and Apparatus. Methyl methacrylate (MMA, 99%), tetraethoxysilane, 3-aminopropyl triethoxysilane (APTES), chloroauric acid ($HAuCl_4 \cdot 4H_2O$), tetramethylolphosphonium chloride, and OVA were purchased from Sigma-Aldrich Co (St. Louis, MO, USA). Potassium persulfate (KPS) (99%) was obtained from J&K Scientific Ltd., China. BSA was bought from Yuanye Co., Ltd., Shanghai, China. The milk was purchased from a local market.

All solvents and chemicals were of analytical reagent and were used without further purification. The slides were immersed in the H_2SO_4/H_2O_2 (7:3, v/v) mixture, and then, the slides were rinsed with deionized water three times. The SEB aptamer sequences were 5′-HS-GGT ATT GAG GGT CGC ATC CAC TGG TCG TTG TTG TCT GTT GTC TGT TAT GTT GTT TCG TGA TGG CTC TAA CTC TCC TCT-3′.

Preparation of PMMA Microspheres. PMMA microspheres were synthesized by emulsion polymerization. A homogeneous mixture of MMA (25 mL) and ultrapure water (125 mL) was heated to 80 °C under mechanical stirring at 300 rpm in a nitrogen atmosphere. Then, KPS (0.3 g, dissolved in 5 mL ultrapure water) was added to the mixture and stirring was continued for 45 min to form an opalescent suspension. The mixture was centrifuged at different speeds to screen the particle size, and finally, it was cleaned and centrifuged at 8000 rpm to collect the white precipitate to obtain the uniform PMMA microspheres.

Preparation of IOPCs. The silica sol was prepared by the co-assembly method. Hydrochloric acid (0.1 M), ethyl orthosilicate, and anhydrous ethanol (mass ratio: 1:1:1.5) were mixed to form a silica sol and incubated under oscillation at room temperature for 1 h. Next, the abovementioned silica sol (90 μL) and 0.9% PMMA microsphere suspension (PMMA: water, 0.9:9.1, v: v) were ultrasonically mixed, and then, the glass slide was inserted vertically into the mixed solution. Then, they were put in an oven at 60 °C for 48 h. With the constant evaporation of deionized water and the hydrolysis of silica sol, the PMMA and silica dioxide were co-assembled on the slide to form a PC film. Essentially, the colloidal assembly induced by evaporation could be thought as a concentration process. In the process, the nanoparticles were tightly packed under the action of van der Waals force, so that the colloidal nanoparticles were arranged neatly.

During a typical calcination process, the temperature increased to 500 °C and maintained for 4 h before falling back to room temperature. After the calcination of PMMA, the colored IOPC was obtained.

Preparation of Au−IOPCs. First, IOPCs were modified by surface amination, as detailed below. IOPCs were immersed in piranha solution for 24 h and washed with ultrapure water and anhydrous ethanol 6 times. The slides were inserted vertically into the glass beakers and dried with nitrogen. Then, 4% of APTES ethanol solution (15 mL) was added into the glass beakers and heated at 70 °C for 6 h. Then, the slides were washed six times with deionized water. The NH_2−IOPC was obtained.

Au NPs at 5−8 nm were prepared by Duff's method.[37] Then, the abovementioned NH_2−IOPC was immersed in the Au NP solution to prepare the Au−IOPC. Meanwhile, the enhancement effect of Au NPs on the IOPC assembled by different sizes of PMMA microspheres was simulated by COMSOL.

Modification of Aptamers on the Au−IOPC. The −SH modified aptamer was diluted with PBS (0.01 M, pH 7.4) to form a storage solution of 10 μM. The Au−IOPC was placed in a glass Petri dish, and the aptamer solution (100 μL) was added onto the Au−IOPC drop by drop. Then, the glass Petri dish was sealed and was placed at 37 °C for 12 h to obtain the Au−Apt IOPC.

A sensing IOPC without Au NPs (CHO−Apt IOPC) was prepared using glutaraldehyde to fix the SEB aptamer on the NH_2−IOPC. The preparation process is as follows: NH_2−IOPC was immersed in the 2.5% glutaraldehyde water solution (mass ratio) for 4 h and then incubated with the SEB aptamer, containing a 5-terminal amino group, to acquire the CHO−Apt IOPC.

Response of the Au−Apt IOPC to SEB. Au−Apt IOPCs were immersed in 10 mL of ultrapure water, and the reflection spectra were obtained through an optical fiber spectrometer at room temperature. After the sensing system reached the equilibrium state (about 30 min), different concentrations of SEB (0.01 fg mL^{-1} to 1000 ng mL^{-1}) were added into the sensing system, and the corresponding reflection spectra were recorded. As a comparison, the CHO−Apt IOPC was also used to detect SEB under the same condition.

Specificity of the Au−Apt IOPC to SEB. Analogues such as SEA, ricin, BSA, and OVA were detected by the Au−Apt IOPC to investigate the specificity of the sensing material. Au−Apt IOPCs were immersed in ultrapure water until the sensing system reached stability. After that, different concentrations of the abovementioned analogues were added, and the corresponding reflection spectra were recorded.

Sample Preparation and Detection. Tap water and milk were chosen as the real sample and spiked with SEB. The newly purchased milk samples were detected by ELISA kit, and the results showed that it contained no SEB. The milk sample was pretreated as follows: they were centrifuged at 5000 rpm for 10 min. After the precipitation was

https://doi.org/10.1021/acsami.1c18386
ACS Appl. Mater. Interfaces 2022, 14, 4637−4646

removed, the remnants were transferred to a new tube and subsequently added with 0.1, 10, and 100 pg mL^{-1} of SEB, respectively. The water sample, without pretreatment, was added with 0.1, 10, and 100 pg mL^{-1} of SEB. The spiked samples were detected using the Au−Apt IOPC method and ELISA kit for comparison.

■ ASSOCIATED CONTENT

Supporting Information

The Supporting Information is available free of charge at https://pubs.acs.org/doi/10.1021/acsami.1c18386.

TEM image of PMMA, UV−vis absorption spectra of Au NPs, XPS of the IOPC, kinetic response of the Au−Apt IOPC, reflection spectra of the IOPC and Au−IOPC, reflection spectra of the Au−IOPC and Au−Apt IOPC responding to SEB, UV absorption spectra of the SEB aptamer before and after the reaction with the Au−IOPC, and optimization of the SEB aptamer concentration reacted with the Au−IOPC (PDF)

■ AUTHOR INFORMATION

Corresponding Authors

Yujing Lian − *College of Food Science and Engineering, Shandong Agricultural University, Tai'an 271018, P. R. China*; Email: yujinglian@sdau.edu.cn

Zhixian Gao − *Tianjin Key Laboratory of Risk Assessment and Control Technology for Environment and Food Safety, Tianjin Institute of Environmental and Operational Medicine, Tianjin 300050, P. R. China*; orcid.org/0000-0003-2818-6671; Email: gaozhx@163.com

Yuan Peng − *Tianjin Key Laboratory of Risk Assessment and Control Technology for Environment and Food Safety, Tianjin Institute of Environmental and Operational Medicine, Tianjin 300050, P. R. China*; orcid.org/0000-0002-4536-4030; Email: dalidao@139.com

Authors

Huijing Shen − *College of Food Science and Engineering, Shandong Agricultural University, Tai'an 271018, P. R. China; Tianjin Key Laboratory of Risk Assessment and Control Technology for Environment and Food Safety, Tianjin Institute of Environmental and Operational Medicine, Tianjin 300050, P. R. China*; orcid.org/0000-0002-9246-1175

Jialei Bai − *Tianjin Key Laboratory of Risk Assessment and Control Technology for Environment and Food Safety, Tianjin Institute of Environmental and Operational Medicine, Tianjin 300050, P. R. China*

Xudong Zhao − *Tianjin Key Laboratory of Risk Assessment and Control Technology for Environment and Food Safety, Tianjin Institute of Environmental and Operational Medicine, Tianjin 300050, P. R. China*

Beibei Lu − *College of Food Science and Engineering, Shandong Agricultural University, Tai'an 271018, P. R. China*

Dianpeng Han − *Tianjin Key Laboratory of Risk Assessment and Control Technology for Environment and Food Safety, Tianjin Institute of Environmental and Operational Medicine, Tianjin 300050, P. R. China*

Shuang Li − *Tianjin Key Laboratory of Risk Assessment and Control Technology for Environment and Food Safety, Tianjin Institute of Environmental and Operational Medicine, Tianjin 300050, P. R. China*; orcid.org/0000-0002-3970-1061

Kang Qin − *Tianjin Key Laboratory of Risk Assessment and Control Technology for Environment and Food Safety, Tianjin Institute of Environmental and Operational Medicine, Tianjin 300050, P. R. China*

Shuyue Ren − *Tianjin Key Laboratory of Risk Assessment and Control Technology for Environment and Food Safety, Tianjin Institute of Environmental and Operational Medicine, Tianjin 300050, P. R. China*

Yu Wang − *Tianjin Key Laboratory of Risk Assessment and Control Technology for Environment and Food Safety, Tianjin Institute of Environmental and Operational Medicine, Tianjin 300050, P. R. China*; orcid.org/0000-0001-7285-8004

Minglin Wang − *College of Food Science and Engineering, Shandong Agricultural University, Tai'an 271018, P. R. China*

Complete contact information is available at: https://pubs.acs.org/10.1021/acsami.1c18386

Author Contributions

#H.S. and J.B. contributed equally. All authors have given approval to the final version of the manuscript.

Notes

The authors declare no competing financial interest.

■ ACKNOWLEDGMENTS

The authors thank the National Key Research and Development Program of China (2018YFC1602600) for funding this research project.

■ DEDICATION

Dedicated to the 100th anniversary of Chemistry at Nankai University.

■ REFERENCES

(1) Liu, F.; Zhang, T.; Mondal, D.; Teng, S.; Zhang, Y.; Huang, K.; Wang, D.; Yang, W.; Mahadevan, P.; Zhao, Y. S.; Xie, R.; Pradhan, N. Light-Emitting Metal-Organic Halide 1D and 2D Structures: Near-Unity Quantum Efficiency, Low-Loss Optical Waveguide and Highly Polarized Emission. *Angew. Chem., Int. Ed.* **2021**, *60*, 13548−13553.

(2) Stein, A.; Li, F.; Denny, N. R. Morphological Control in Colloidal Crystal Templating of Inverse Opals, Hierarchical Structures, and Shaped Particles. *Chem. Mater.* **2008**, *20*, 649−666.

(3) Su, K.-H.; Wei, Q.-H.; Zhang, X.; Mock, J. J.; Smith, D. R.; Schultz, S. Interparticle Coupling Effects on Plasmon Resonances of Nanogold Particles. *Nano Lett.* **2003**, *3*, 1087−1090.

(4) Cai, Z.; Liu, Y. J.; Lu, X.; Teng, J. In Situ "Doping" Inverse Silica Opals with Size-Controllable Gold Nanoparticles for Refractive Index Sensing. *J. Phys. Chem. C* **2013**, *117*, 9440−9445.

(5) Cai, Z.; Liu, Y. J.; Teng, J.; Lu, X. Fabrication of Large Domain Crack-free Colloidal Crystal Heterostructures with Superposition Bandgaps Using Hydrophobic Polystyrene Spheres. *ACS Appl. Mater. Interfaces* **2012**, *4*, 5562−5569.

(6) Cai, Z.; Teng, J.; Yan, Q.; Zhao, X. S. Solvent Effect on the Self-assembly of Colloidal Microspheres via a Horizontal Deposition Method. *Colloids Surf., A* **2012**, *402*, 37−44.

(7) Yakubovsky, D. I.; Stebunov, Y. V.; Kirtaev, R. V.; Voronin, K. V.; Voronov, A. A.; Arsenin, A. V.; Volkov, V. S. Graphene-Supported Thin Metal Films for Nanophotonics and Optoelectronics. *Nanomaterials* **2018**, *8*, 1058.

(8) Beadie, G.; Brindza, M.; Flynn, R. A.; Rosenberg, A.; Shirk, J. S. Refractive Index Measurements of Poly(methyl methacrylate) (PMMA) from 0.4-1.6 μm. *Appl. Opt.* **2015**, *54*, F139−F143.
(9) Mu, Z.; Zhao, X.; Huang, Y.; Lu, M.; Gu, Z. Photonic Crystal Hydrogel Enhanced Plasmonic Staining for Multiplexed Protein Analysis. *Small* **2015**, *11*, 6036−6043.
(10) Sun, T.; Zhao, Z.; Liu, W.; Xu, Z.; He, H.; Ning, B.; Jiang, Y.; Gao, Z. Development of Sandwich Chemiluminescent Immunoassay Based on an Anti-staphylococcal Enterotoxin B Nanobody-Alkaline Phosphatase Fusion Protein for Detection of Staphylococcal Enterotoxin B. *Anal. Chim. Acta* **2020**, *1108*, 28−36.
(11) Hatton, B.; Mishchenko, L.; Davis, S.; Sandhage, K. H.; Aizenberg, J. Assembly of Large-area, Highly Ordered, Crack-free Inverse Opal Films. *Proc. Natl. Acad. Sci. U.S.A.* **2010**, *107*, 10354−10359.
(12) Wu, D.; Xu, F.; Sun, B.; Fu, R.; He, H.; Matyjaszewski, K. Design and Preparation of Porous Polymers. *Chem. Rev.* **2012**, *112*, 3959−4015.
(13) Feng, Y.; Wang, B.; Tian, Y.; Chen, H.; Liu, Y.; Fan, H.; Wang, K.; Zhang, C. Active Fluidic Chip Produced using 3D-Printing for Combinatorial Therapeutic Screening on Liver Tumor Spheroid. *Biosens. Bioelectron.* **2020**, *151*, 111966.
(14) Inan, H.; Poyraz, M.; Inci, F.; Lifson, M. A.; Baday, M.; Cunningham, B. T.; Demirci, U. Photonic Crystals: Emerging Biosensors and Their Promise for Point-of-care Applications. *Chem. Soc. Rev.* **2017**, *46*, 366−388.
(15) Fenzl, C.; Hirsch, T.; Wolfbeis, O. S. Photonic crystals for chemical sensing and biosensing. *Angew. Chem., Int. Ed.* **2014**, *53*, 3318−3335.
(16) Das, R.; Landis, R. F.; Tonga, G. Y.; Cao-Milán, R.; Luther, D. C.; Rotello, V. M. Control of Intra-versus Extracellular Bioorthogonal Catalysis Using Surface-Engineered Nanozymes. *ACS Nano* **2019**, *13*, 229−235.
(17) Zhang, X.; Liu, S.; Song, X.; Wang, H.; Wang, J.; Wang, Y.; Huang, J.; Yu, J. Robust and Universal SERS Sensing Platform for Multiplexed Detection of Alzheimer's Disease Core Biomarkers Using PAapt-AuNPs Conjugates. *ACS Sens.* **2019**, *4*, 2140−2149.
(18) Liu, J.; Jalali, M.; Mahshid, S.; Wachsmann-Hogiu, S. Are Plasmonic Optical Biosensors Ready for Use in Point-of-Need Applications? *Analyst* **2020**, *145*, 364−384.
(19) Li, Z.; Leustean, L.; Inci, F.; Zheng, M.; Demirci, U.; Wang, S. Plasmonic-Based Platforms for Diagnosis of Infectious Diseases at the Point-of-care. *Biotechnol. Adv.* **2019**, *37*, 107440.
(20) Mejía-Salazar, J. R.; Oliveira, O. N. Plasmonic Biosensing Focus Review. *Chem. Rev.* **2018**, *118*, 10617−10625.
(21) Said, D. A.; Ali, A. M.; Khayyat, M. M.; Boustimi, M.; Loulou, M.; Seoudi, R. A Study of the Influence of Plasmonic Resonance of Gold Nanoparticle Doped PEDOT: PSS on the Performance of Organic Solar Cells Based on CuPc/C6(0). *Heliyon* **2019**, *5*, No. e02675.
(22) Tavares, A. P. M.; Truta, L. A. A. N. A.; Moreira, F. T. C.; Minas, G.; Sales, M. G. F. Photovoltaics, Plasmonics, Plastic Antibodies and Electrochromism Combined for a Novel Generation of Self-Powered and Self-Signalled Electrochemical Biomimetic Sensors. *Biosens. Bioelectron.* **2019**, *137*, 72−81.
(23) Zhang, Z.; Zhang, L.; Hedhili, M. N.; Zhang, H.; Wang, P. Plasmonic Gold Nanocrystals Coupled with Photonic Crystal Seamlessly on TiO2 Nanotube Photoelectrodes for Efficient Visible Light Photoelectrochemical Water Splitting. *Nano Lett.* **2013**, *13*, 14−20.
(24) Shen, W.; Li, M.; Wang, B.; Liu, J.; Li, Z.; Jiang, L.; Song, Y. Hierarchical Optical Antenna: Gold Nanoparticle-Modified Photonic Crystal for Highly-Sensitive Label-Free DNA Detection. *J. Mater. Chem.* **2012**, *22*, 8127−8133.
(25) Hollams, E. M.; Hales, B. J.; Bachert, C.; Huvenne, W.; Parsons, F.; de Klerk, N. H.; Serralha, M.; Holt, B. J.; Ahlstedt, S.; Thomas, W. R.; Sly, P. D.; Holt, P. G. Th2-Associated Immunity to Bacteria in Teenagers and Susceptibility to Asthma. *Eur. Respir. J.* **2010**, *36*, 509−516.
(26) Hudson Reichenberg, L. C.; Garg, R.; Fernalld, R.; Bost, K. L.; Piller, K. J. Systemic Cytokine and Chemokine Responses in Immunized Mice Challenged with Staphylococcal Enterotoxin B. *Toxicon* **2017**, *133*, 82−90.
(27) Fang, J.; Zhou, C.; Chen, Y.; Fang, L.; Wang, W.; Zhu, C.; Ni, Y.; Lu, C. Efficient Photocatalysis of Composite Films Based on Plasmon-Enhanced Triplet-Triplet Annihilation. *ACS Appl. Mater. Interfaces* **2020**, *12*, 717−726.
(28) Yan, D.; Qiu, L.; Shea, K. J.; Meng, Z.; Xue, M. Dyeing and Functionalization of Wearable Silk Fibroin/Cellulose Composite by Nanocolloidal Array. *ACS Appl. Mater. Interfaces* **2019**, *11*, 39163−39170.
(29) Ye, L.; Wen, G.; Ouyang, H.; Liu, Q.; Liang, A.; Jiang, Z. A Novel and Highly Sensitive Nanocatalytic Surface Plasmon Resonance-Scattering Analytical Platform for Detection of Trace Pbions. *Sci. Rep.* **2016**, *6*, 24150.
(30) Johnson, P. B.; Christy, R. W. Optical Constants of the Noble Metals. *Phys. Rev. B* **1972**, *6*, 4370−4379.
(31) Gao, L.; Lemarchand, F.; Lequime, M. Refractive index determination of SiO2 layer in the UV/Vis/NIR Range: Spectrophotometric Reverse Engineering on Single and Bi-layer Designs. *J. Eur. Opt. Soc.-Rapid Publ.* **2013**, *8*, 13010.
(32) Endo, T.; Ozawa, S.; Okuda, N.; Yanagida, Y.; Tanaka, S.; Hatsuzawa, T. Reflectometric Detection of Influenza Virus in Human Saliva Using Nanoimprint Lithography-based Flexible Two-dimensional Photonic Crystal Biosensor. *Sens. Actuators, B* **2010**, *148*, 269−276.
(33) Wu, E.; Peng, Y.; Zhang, X.; Bai, J.; Song, Y.; He, H.; Fan, L.; Qu, X.; Gao, Z.; Liu, Y.; Ning, B. Ultrasensitive Sensing Material Based on Opal Photonic Crystal for Label-Free Monitoring of Transferrin. *ACS Appl. Mater. Interfaces* **2017**, *9*, 5778−5783.
(34) Sospedra, I.; Soler, C.; Mañes, J.; Soriano, J. M. Rapid Whole Protein Quantitation of Staphylococcal Enterotoxins A and B by Liquid Chromatography/Mass Spectrometry. *J. Chromatogr. A* **2012**, *1238*, 54−59.
(35) Nia, Y.; Rodriguez, M.; Zeleny, R.; Herbin, S.; Auvray, F.; Fiebig, U.; Avondet, M. A.; Munoz, A.; Hennekinne, J. A. Organization and ELISA-Based Results of the First Proficiency Testing to Evaluate the Ability of European Union Laboratories to Detect Staphylococcal Enterotoxin Type B (SEB) in Buffer and Milk. *Toxins* **2016**, *8*, 268.
(36) Slavík, R.; Homola, J.; Brynda, E. A Miniature Fiber Optic Surface Plasmon Resonance sensor for Fast Detection of Staphylococcal Enterotoxin B. *Biosens. Bioelectron.* **2002**, *17*, 591−595.
(37) Duff, D. G.; Baiker, A.; Edwards, P. P. A New Hydrosol of Gold Clusters. 1. Formation and Particle Size Variation. *Langmuir* **1993**, *9*, 2301−2309.

https://doi.org/10.1021/acsami.1c18386
ACS Appl. Mater. Interfaces 2022, 14, 4637−4646